Published paper
Gaskell, P.H., Jimack, P.K., Sellier, M. and Thompson, H.M. (2006) *Flow of evaporating, gravity-driven thin liquid films over topography.* Physics of Fluids, 18 (Art. No. 013601).

Flow of evaporating, gravity-driven thin liquid films over topography

by

P.H. Gaskell [a], P.K. Jimack [b], M. Sellier [c] and H.M Thompson [a]

[a] School of Mechanical Engineering

[b] School of Computing

The University of Leeds, Leeds LS2 9JT, UK

[c] Fraunhofer-Institut fuer Techno- und Wirtschaftsmathematik

Gottlieb-Daimler-Strasse, Geb. 49, 67 663 Kaiserslautern, Germany

Abstract

The effect of topography on the free surface and solvent concentration profiles of an evaporating thin film of liquid flowing down an inclined plane is considered. The liquid is assumed to be composed of a resin dissolved in a volatile solvent with the associated solvent concentration equation derived on the basis of the well-mixed approximation. The dynamics of the film is formulated as a lubrication approximation and the effect of a composition-dependent viscosity is included in the model. The resulting time-dependent, non-linear, coupled set of governing equations is solved using a Full Approximation Storage multigrid method. The approach is first validated against a closed-form analytical solution for the case of a gravity-driven, evaporating thin film flowing down a flat substrate. Analysis of the results for a range of topography shapes reveal that while a full-width, spanwise topography such as a step-up or a step-down does not appear to affect the composition of the film, the same is no longer true for the case of localised topography, such as a peak or a trough, for which clear non-uniformities of the solvent concentration profile can be observed in the wake of the topography.

Keywords: thin film, solvent evaporation, topography, multigrid

I Introduction

Several industrial processes require thin films to flow, under the action of body forces, over substrates with topographic features caused, for example, either by direct patterning or by defects in the substrate. Typical examples include paints or photoresist films, used in the lithographic stages of the manufacture of microelectronic components[1]. Such flows have received considerable attention in the literature, the focus until recently having been primarily on flow over one-dimensional topographies. Several such studies, see for example[2−4], have investigated the effect of the topography and governing parameters on continuous thin films over combinations of step-down and step-up topographies, with particular emphasis on the formation and stability of the Capillary ridge located just upstream of a step-down topography. These analyses have since been extended to consider the effect of inertia and intermolecular forces[5] and to consider the motion of discontinuous thin films with contact lines over substrates containing trench or wedge topographies[6].

Due to the formidable experimental and theoretical challenges involved, fully three-dimensional flow over topography has received far less attention in the literature to date. Hayes, O'Brien & Lammers[7], for example, formulated a Green's function approach which enables the free surface to be calculated successfully for flows over shallow, arbitrary topographies, while Bielarz & Kalliadasis[5] employed the popular alternating direction implicit *time-splitting* approach used by Schwartz and co-workers[8−9] to solve for the flow over a square mound. In contrast, Gaskell et al[10] developed a Multigrid approach with adaptive time-stepping for the efficient numerical solution of the nonlinear lubrication equations as an alternative to time-splitting and used it successfully to solve the problems of droplet spreading on a surface with a well-defined topography and the flow of continuous, thin water films down an inclined plane containing a range of topographies[11]. The latter had recently been investigated experimentally using phase-stepped interferometry by Decré and Baret[1].

A detailed comparison between experiment and Finite Element solutions of the full Navier-Stokes equations for one-dimensional topographies[11] has quantified the accuracy of the lubrication approach and shown the solution of the governing equations to be accurate even when the assumptions on which they are based are not strictly satisfied. Multigrid solutions to fully three-dimensional flows are also found to agree well with experiment[1] and show that the characteristic horseshoe-shaped *bow* wave, downstream of

a localised topography, can be well-represented by an inverse hyperbolic cosine function. The simulations similarly supported the experimental findings that the free surface response for shallow topographies is approximately linear.

Although the above studies on flow past topographies have assumed that the liquids are pure substances, in many practical situations the liquid is composed of a functional resin dissolved in a volatile solvent. The latter, when subsequently evaporated, leaves a solid resin film on the substrate[9]. The motivation therefore of the present work is to study how flow past topography is affected by solvent evaporation and, in turn, how the topography affects the composition of the resin/solvent mixture.

Despite few previous studies on evaporative flow over topography having appeared in the literature, such flows over flat or curved substrates have been widely investigated, revealing a range of interesting phenomena. Overdiep's experiments[12], for example, showed that the free surface of some solvent-based high-gloss alkyd paints unexpectedly undergo reversal after the levelling of disturbances; that is, initial peaks in the free surface become troughs and vice versa. This phenomenon was later analysed theoretically by Eres et al[13] who solved a three-dimensional lubrication model of the flow numerically and confirmed that reversal is caused by the solutal Marangoni effect due to variations in solvent concentration which in turn lead to surface tension gradients. The latter study was one of several by Schwartz and co-workers who have modelled the effects of solvent evaporation in applications ranging from the role of surface tension gradients in correcting corner defects[14] and in crater formation[15], to the effect of viscosity increase due to solvent depletion on droplet reticulation[9].

Other studies of flow over planar substrates of relevance to the present work include the recent analysis of evaporation in gravity-driven flow of a discontinuous, thin liquid film with a dynamic contact line[16] and, in particular, that of Meyerhofer[17] which is credited as being the first attempt to model the effects of solvent evaporation and the associated viscosity rise on the thickness of dried films during spin coating. Using a one-dimensional, axisymmetric model for film thickness and solvent concentration, he proposed that film thinning in spin coating occurs in two distinct stages. At first, the effect of evaporation is negligible and the film thins mainly by centrifugally-driven flow toward the edge of the substrate. During the second stage, solvent evaporation becomes the dominant mechanism for film thinning as the viscosity rise due to solvent evaporation reduces the radial outflow significantly.

Meyerhofer's model was subsequently extended to consider the effects of solvent concentration *across* the film[18], although still in the context of a one-dimensional analysis. The two-stage assumption of Meyerhofer was later used by Stillwagon and Larson[19] in a lubrication analysis to predict the free surface profile of a drying spin coated film over topography. Their model for the initial, flow-dominated stage was unable to predict how the topography affects the solvent concentration and, the excellent agreement between their theory and experiment showed that such effects are small in the context of spin coating.

The present study similarly focuses on the initial stages of the flow during which the viscosity increases due to solvent concentration, but in the different context of constant flux gravity-driven flow of a continuous, thin film down an inclined plane with topography. The flow is clearly different from that of centrifugally-driven flow but the mathematical framework in the context of the lubrication approximation differs only in terms of the nature of a dimensionless number - see eq. (5) of reference 19. This follows in that for spin coating it is customary to: (i) ignore the axisymmetry of the flow if a topography is sufficiently far from the axis of symmetry; (ii) adopt a quasi-steady analysis by treating the flux as constant since the rearrangement of fluid over a topography occurs much faster than any associated film thinning due to the presence of a non-constant flux - see also references 20 and 21.

Section 2 describes the flow under consideration together with the analytical and numerical lubrication models, both of which employ the assumption that the resin and solvent are *well-mixed*. A brief overview of the solution methodology then follows since a detailed description of the multigrid approach on which it is based is already available[10]. Results, in ascending order of complexity, then follow. First, the analytical solution for the two-dimensional flow (i.e. invariant in the spanwise direction) of an evaporating thin liquid film down a flat inclined plane is derived, following on from Huppert's earlier analytical solution for the non-evaporating case[22]. This analysis reveals that the free surface can exhibit three distinct types of behaviour, dependant on the evaporation rate and how steeply viscosity increases with evaporative solvent loss. This analytical solution provides a convenient reference by which to assess the effect of a step-down and a trench topography on the solvent concentration and is used to validate the numerical predictions. Results for the fully three-dimensional flow of an evaporating film down an inclined plane over localised topographies are then presented and compared with corresponding solutions without solvent evaporation.

II Problem formulation

In the context of thin liquid films the fact that the ratio $\varepsilon = \frac{H_0}{L}$ is small, where H_0 is the characteristic film thickness and L the characteristic length in the streamwise direction, can be exploited to reduce the general governing Navier-Stokes equations to a more tractable coupled pair of second order nonlinear partial differential equations in terms of the film thickness, H, and the pressure across the film, P. This approach, commonly referred to as the lubrication or long-wave approximation, has been used successfully by a number of authors to model a variety of thin film flows[23]. For the particular case of gravity-driven, non-evaporative flow over topographies its accuracy has recently been quantified[11].

A. Governing Equations

The case of flow of a continuous film of liquid, of constant flux Q_0, over a surface (lateral extent L and span width W) containing distinct topographic features and inclined at an angle α to the horizontal is illustrated in Figure 1, which shows the notation adopted and the accompanying coordinate system. Each well-defined topographical feature has amplitude S_0 and form $S(X,Y)$, with lateral extent L_T and span width W_T, centred at (X_T, Y_T). These features may completely span the domain (in which case $W_T = W$ and $L_T \ll L$, leading to two-dimensional flow), or be localised (i.e. $W_T \ll W$ and $L_T \ll L$, giving three-dimensional flow). Each topography may either be a depression ($S_0 < 0$) or a protrusion ($S_0 > 0$).

The liquid is assumed incompressible and Newtonian, with constant density ρ and surface tension σ. The solvent concentration $c_s = h_s/h$ is defined by the ratio of the imaginary thickness of the solvent layer, h_s, to the total film thickness h[13] and, following previous studies[9,13,14], the viscosity μ is assumed to depend exponentially on c_s, obeying:

$$\mu = \mu_0 e^{a(c_0 - c_s)} , \tag{1}$$

where μ_0 is the reference value of the concentration-dependent dynamic viscosity and c_0 is the initial solvent concentration. The parameter a controls the sensitivity of the viscosity to solvent concentration variations; its form ensures that the viscosity effectively precludes flow for small solvent concentrations.

Since the flows under consideration are for the case α not too small, a natural choice of characteristic film

thickness is that commensurate with fully developed film flow[11], viz

$$H_0 = \left(\frac{3\mu_0 Q_0}{\rho g \sin\alpha}\right)^{1/3}, \tag{2}$$

while the extent of the substrate, L, is equal to β times the dynamic capillary length, L_d, viz:

$$L = \beta L_d \quad \text{where} \quad L_d = \left(\frac{\sigma H_0}{3\rho g \sin\alpha}\right)^{1/3} = \frac{H_0}{6Ca^{1/3}}\,. \tag{3}$$

Here, $Ca = \frac{\mu_0 U_0}{\sigma}$, is the Capillary number expressing the ratio of viscous to surface tension stresses. Unless otherwise stated, β is chosen to be equal to 50, a large enough value to ensure that the free surface relaxes to its undisturbed shape downstream of the topography.

The characteristic velocity U_0 is taken to be the free surface velocity of the fully developed film, namely:

$$U_0 = \frac{3Q_0}{2H_0}\,, \tag{4}$$

while the characteristic pressure and time scale are $P_0 = \frac{\rho g L \sin\alpha}{2}$ and $T_0 = \frac{L}{U_0}$, respectively.

Based upon these scalings, the following dimensionless variables:

$$\begin{aligned} h(x,y,t) &= \frac{H}{H_0},\ s(x,y) = \frac{S}{H_0},\ \tilde{\mu} = \frac{\mu}{\mu_0},\ (x,y) = \frac{(X,Y)}{L}, \\ z &= \frac{Z}{H_0},\ p(x,y,t) = \frac{P}{P_0},\ (u,v,\varepsilon w) = (U,V,W)\frac{1}{U_0},\ t = \frac{T}{T_0}\,, \end{aligned} \tag{5}$$

when introduced into the Navier-Stokes equations, and retaining leading-order terms (those up to $O(\varepsilon^2, \varepsilon^2 Re)$) yields the following mass conservation equation:

$$\frac{\partial h}{\partial t} + \nabla.\underline{Q} + e = 0\,, \tag{6}$$

where $e = E/(\varepsilon U_0)$ is the constant, dimensionless, evaporation rate and the flux vector $\underline{Q}$ is defined as $(Q_x, Q_y)^T = \int_s^{h+s} (u,v)^T\, dz$. The evaporation rate E has the dimensions of a velocity (the rate of thinning of a flat film) and is chosen to be constant since only small variations of the solvent concentration are considered. More sophisticated evaporation models would be required for larger variations such as the

power law proposed in Schwartz et al[9].

Applying a no-slip boundary condition at the surface of the solid substrate and assuming negligible shear stress at the liquid-air interface yields:

$$Q_x = -\frac{h^3}{3\tilde{\mu}}\left(\frac{\partial p}{\partial x} - 2\right), \tag{7}$$

$$Q_y = -\frac{h^3}{3\tilde{\mu}}\left(\frac{\partial p}{\partial y}\right), \tag{8}$$

which, when combined with equation (6), gives

$$\frac{\partial h}{\partial t} = \frac{\partial}{\partial x}\left[\frac{h^3}{3\tilde{\mu}}\left(\frac{\partial p}{\partial x} - 2\right)\right] + \frac{\partial}{\partial y}\left[\frac{h^3}{3\tilde{\mu}}\left(\frac{\partial p}{\partial y}\right)\right] - e. \tag{9}$$

The pressure across the film results from contributions from the surface tension and the hydrostatic pressure:

$$p = -\frac{6}{\beta^3}\nabla^2(h+s) + \frac{2}{\beta}6^{1/3}N(h+s), \tag{10}$$

where $\nabla^2(h+s)$ is the small slope approximation to the free surface curvature and $N = Ca^{1/3}\cot\alpha$ measures the relative importance of the normal component of gravity[24].

As pointed out by Howison et al[25], one of the key parameters dictating the choice of evaporation model is the diffusivity of the solvent. If the diffusion of solvent is sufficiently rapid, the leading-order distribution of solvent across the film is uniform, leading to the so-called *well-mixed* assumption[9]. This assumption fits naturally within the lubrication formalism for which all quantities are depth averaged and has been used successfully to predict the formation of defects in drying films[9,15]. If the *well-mixed* assumption is violated, variations of the solvent concentration across the film have to be taken into account and it is not possible to remain within the framework of the lubrication approximation unless the fluid parameters (viscosity, surface tension) are assumed constant across the film[26]. Howison et al[25] discussed the validity of the *well-mixed* approximation and showed it to be valid provided the characteristic time for the solvent to diffuse across the film, $t_d^{across} = H_0^2/D$, is much smaller than that for the fluid to flow across the film, $t_f^{across} = H_0/\varepsilon U_0$, leading to the condition $D >> \varepsilon^2 L U_0$. They showed further that, to O(ε), the equation

for solvent conservation is given by

$$\frac{\partial (hc_s)}{\partial t} + \nabla . \left(c_s \underline{Q} \right) = -e + d\nabla . \left(h \nabla c_s \right) \ , \tag{11}$$

where $d = D/LU_0$ is the dimensionless solvent diffusivity. Combining equation (11) with equations (6), (7) and (8) yields:

$$\frac{\partial c_s}{\partial t} = \left[\frac{h^2}{3\tilde{\mu}} \left(\frac{\partial p}{\partial x} - 2 \right) \right] \frac{\partial c_s}{\partial x} + \left[\frac{h^2}{3\tilde{\mu}} \left(\frac{\partial p}{\partial y} \right) \right] \frac{\partial c_s}{\partial y} + e \frac{(c_s - 1)}{h} + \frac{d}{h} \nabla . \left(h \nabla c_s \right) \ , \tag{12}$$

where $\tilde{\mu} = \mu/\mu_0$ is the viscosity ratio at a given solvent concentration. Howison et al[25] showed also that the lateral diffusion in equations (11) and (12) is dominated by convection provided $D \ll LU_0$, in which case equation (12) reduces to:

$$\frac{\partial c_s}{\partial t} = \left[\frac{h^2}{3\tilde{\mu}} \left(\frac{\partial p}{\partial x} - 2 \right) \right] \frac{\partial c_s}{\partial x} + \left[\frac{h^2}{3\tilde{\mu}} \left(\frac{\partial p}{\partial y} \right) \right] \frac{\partial c_s}{\partial y} + e \frac{(c_s - 1)}{h} \ . \tag{13}$$

Before discussing appropriate boundary conditions for the evolution equations (9), (10) and (13), their validity for the results presented below is assessed by considering a realistic example. In Table 1, representative solvent/resin properties[9,25] have been used to calculate maximum and minimum values for the associated scalings and dimensionless groups for the case of a 70 μm thick film flowing down a plane inclined at 30^o to the horizontal with physical properties in the ranges $0.001\text{Pas} \leq \mu \leq 0.5\text{Pas}$, $0.02\text{Nm}^{-1} \leq \sigma \leq 0.05\text{Nm}^{-1}$, 10^{-8} ms$^{-1} \leq E \leq 10^{-6}$ ms^{-1}, and 10^{-9} m^{2}s$^{-1} \leq D \leq 10^{-7}$ m^{2}s^{-1} and with a substrate that extends over 50 Capillary lengths ($\beta = 50$). Note that in practice D is a strongly varying function of solvent concentration which may change by several orders of magnitude as the solvent concentration varies[25].

As discussed above, the twin assumptions that the solvent is *well-mixed* and that lateral diffusion is negligible, required to obtain equation (13), are valid provided $\varepsilon^2 \ll d \ll 1$; Table 1 shows that this condition is met except for thick films with very small viscosity and diffusivity. All subsequent results employ the data set: $\mu_0 = 0.025$ Pa s, $\rho = 1000$ kg m^{-3}, $\sigma = 0.035$ N m^{-1}, $D = 10^{-8}$ m^2 s^{-1} and 10^{-8} m s$^{-1} \leq E \leq 10^{-6}$ m s^{-1} (i.e. $0.008 \leq e \leq 0.8$). The corresponding scalings and dimensionless groups used in the computations are also shown in Table 1; the well-mixed condition $\varepsilon^2 \ll d \ll 1$ being satisfied in all cases.

Consider now the assumption used in deriving equation (9) that the surface tension is constant. According to Howison et al[25] the characteristic in plane velocity for flows driven by surface tension gradients is $U_g = \frac{\varepsilon \Delta c_s \Delta\sigma}{\mu_0}$, where Δc_s denotes a characteristic measure of the variation in solvent concentration and $\Delta\sigma$ the difference between the surface tension of pure resin and that of pure solvent. Since $\Delta\sigma$ is usually $O(10^{-2})$ and Δc_s is also $O(10^{-2})$, Table 1 also shows that for the results presented below, $U_g \ll U_0$ so that Marangoni effects can indeed be neglected.

B. Boundary and initial conditions

At the upstream boundary, $x = 0$, the assumption of fully developed flow yields

$$h(x=0,y) = 1 \ , \ c_s(x=0,y) = c_0 \ \text{ and } \ \frac{\partial p}{\partial x}(x=0,y) \ = 0. \tag{14}$$

Along the streamwise boundaries, $y = 0$ and $y = 1$, the spanwise gradients in h and p are zero to impose zero spanwise flux. Since solvent depletion causes film thickening due to the associated increases in viscosity, at the downstream boundary, $x = 1$, the conditions there are chosen to allow a non-zero free surface slope:

$$\frac{\partial^2 h}{\partial x^2}(x=1,y) = \ \frac{\partial p}{\partial x}(x=1,y) = 0. \tag{15}$$

Initially, the free surface is prescribed to be flat ($h(x,y,t=0) + s(x,y) = 1$) with a uniform solvent concentration c_0, although the specific choice of initial conditions is found to be unimportant in practice since the same steady-state is reached for all initial conditions tried.

Equations (6), (10) and (13) constitute the governing equations for the dependent unknowns $h(x,y,t)$, $p(x,y,t)$ and $c_s(x,y,t)$ and these are fully defined for specific values of a, c_0, β, N and e. The numerical scheme for solving them is based on the $\mathcal{FAS}$ multigrid method and is outlined briefly below, but the interested reader is directed to the pioneering work of Brandt[27,28] for an in depth overview of the method and to recent references in relation to its specific application to non-evaporating thin film flow problems[10,29].

III Method of solution

Solutions are sought on a square computational domain with $(x,y) \in \Omega = (0,1) \times (0,1)$ and a uniform mesh having $(2^{k_f}+1)$ nodes in each direction. The discrete analogue of eqs. (6), (10) and (13) are obtained using central differences, leading to the following second order accurate spatial discretisations

$$\begin{aligned}\frac{\partial h_{i,j}}{\partial t} &= \frac{1}{\Delta^2}\left[\frac{h^3}{3\tilde{\mu}}|_{i+\frac{1}{2},j}\left(p_{i+1,j}-p_{i,j}\right) - \frac{h^3}{3\tilde{\mu}}|_{i-\frac{1}{2},j}\left(p_{i,j}-p_{i-1,j}\right) + \right. \\ &\quad \left. \frac{h^3}{3\tilde{\mu}}|_{i,j+\frac{1}{2}}\left(p_{i,j+1}-p_{i,j}\right) - \frac{h^3}{3\tilde{\mu}}|_{i,j-\frac{1}{2}}\left(p_{i,j}-p_{i,j-1}\right)\right] - \\ &\quad 2h_{i,j}^2\left(\frac{h_{i+1,j}-h_{i-1,j}}{2\Delta}\right) - e + O(\Delta^2)\,, \end{aligned} \tag{16}$$

$$\begin{aligned} & p_{i,j} + \frac{6}{\beta^3\Delta^2}\left[(h_{i+1,j}+s_{i+1,j}) + (h_{i-1,j}+s_{i-1,j}) + (h_{i,j+1}+s_{i,j+1}) + \right. \\ & \left. (h_{i,j-1}+s_{i,j-1}) - 4(h_{i,j}+s_{i,j})\right] - \frac{2}{\beta}6^{1/3}N(h_{i,j}+s_{i,j}) + O(\Delta^2) = 0\,, \end{aligned} \tag{17}$$

$$\begin{aligned}\frac{\partial c_{si,j}}{\partial t} &= \frac{h_{i,j}^2}{12\tilde{\mu}_{i,j}\Delta^2}\left[\left(p_{i+1,j}-p_{i-1,j}\right)\left(c_{si+1,j}-c_{si-1,j}\right) + \right. \\ &\quad \left.\left(p_{i,j+1}-p_{i,j-1}\right)\left(c_{si,j+1}-c_{si,j-1}\right)\right] - \frac{h_{i,j}^2}{3\tilde{\mu}_{i,j}\Delta}\left(c_{si+1,j}-c_{si-1,j}\right) + \\ &\quad e\frac{\left(c_{si,j}-1\right)}{h_{i,j}} + O(\Delta^2)\,, \end{aligned} \tag{18}$$

for any interior point (i,j) in the computational domain, where $\Delta = 2^{-k_f}$ is the spatial increment. The mid-point interpolation of the prefactors $\Gamma(h) = \frac{h^3}{3\tilde{\mu}}$ in eq. (16) simply consists of a linear interpolation of the prefactor between the two neighbouring nodes, viz

$$\frac{h^3}{3\tilde{\mu}}|_{i\pm\frac{1}{2},j} = \frac{1}{2}\left(\frac{h^3}{3\tilde{\mu}}|_{i\pm1,j} + \frac{h^3}{3\tilde{\mu}}|_{i,j}\right)\,, \tag{19}$$

with analogous expressions for $\frac{h^3}{3\tilde{\mu}}|_{i,j\pm\frac{1}{2}}$.

The standard implicit, second order accurate Crank-Nicholson scheme is used to approximate the time

derivatives in eqs. (16) and (18). The implicit nature of the scheme ensures the stability of the time integration. Accordingly, eqs. (16) and (18) are rewritten as follows,

$$h_{i,j}^{n+1} - \frac{1}{2}\Delta t^{n+1} F^{n+1} = h_{i,j}^{n} + \frac{1}{2}\Delta t^{n+1} F^{n} , \tag{20}$$

$$c_{s_{i,j}}^{n+1} - \frac{1}{2}\Delta t^{n+1} G^{n+1} = c_{s_{i,j}}^{n} + \frac{1}{2}\Delta t^{n+1} G^{n} , \tag{21}$$

where F^n and G^n correspond respectively to the right-hand side of eqs. (16) and (18) (excluding the remainder terms) at the n^{th} time step. Consequently, at each time step it is necessary to solve the coupled nonlinear system given by equations (20), (17) and (21) at each grid point (i, j). This may be written in the following condensed form:

$$L_{k_f}^{h}\left(\underline{h}_{k_f}^{n+1}, \underline{p}_{k_f}^{n+1}, \underline{c_s}_{k_f}^{n+1}\right) = f_{k_f}^{h}\left(\underline{h}_{k_f}^{n}, \underline{p}_{k_f}^{n}, \underline{c_s}_{k_f}^{n}\right) , \tag{22}$$

$$L_{k_f}^{p}\left(\underline{h}_{k_f}^{n+1}, \underline{p}_{k_f}^{n+1}\right) = 0 , \tag{23}$$

$$L_{k_f}^{c_s}\left(\underline{h}_{k_f}^{n+1}, \underline{p}_{k_f}^{n+1}, \underline{c_s}_{k_f}^{n+1}\right) = f_{k_f}^{c_s}\left(\underline{h}_{k_f}^{n}, \underline{p}_{k_f}^{n}, \underline{c_s}_{k_f}^{n}\right) , \tag{24}$$

where $f_{k_f}^{h}$ and $f_{k_f}^{c_s}$ correspond to the right-hand side of eqs. (20) and (21) respectively.

The solution scheme employed for this large algebraic system is based upon a straightforward generalization of the multigrid procedure described in Gaskell et al[10]. This multigrid algorithm requires a small number of iterations of a nonlinear Gauss-Seidel solver to be taken on the finest grid, with $(2^{k_f}+1)$ nodes in each direction, and then both this "pre-smoothed" solution and the corresponding residuals are restricted to a coarser grid. A "coarse grid correction" problem is then solved on this mesh and the computed corrections to h, p and c_s are interpolated back to the fine mesh. The latest fine grid solution is then updated and a small number of further Gauss-Seidel iterations are taken (the "post-smooths"). Note that the coarser grid problem may itself be solved by the same process of taking a small number of pre-smooths, a still coarser grid correction and then some post smooths. At the coarsest grid encountered a different solution procedure is required; for this work (unlike in Gaskell et al[10]) simply a large number of nonlinear Gauss-Seidel iterations are used, leading to satisfactory solutions provided the grid is sufficiently coarse (e.g. 9 nodes in each direction). This whole process is referred to as a single V-cycle and may be repeated numerous times until convergence on the finest grid is achieved.

In order to describe the nonlinear Gauss-Seidel smoother used in this work, consider the equations that must be solved at an arbitrary grid level, level k say. These equations always take the same form as (22) to (24) however Δ is now equal to 2^{-k} and the coarse grid correction causes a modification to the right-hand sides when $k < k_f$ (see Gaskell et al[10] or Trottenberg et al[30] for full details). Hence, at each node (i, j) on level k, these equations may be expressed as

$$[L_k^h\left(\underline{h}_k^{n+1}, \underline{p}_k^{n+1}, \underline{c_s}_k^{n+1}\right)]_{ij} = [f_k^h]_{ij}\,, \tag{25}$$

$$[L_k^p\left(\underline{h}_k^{n+1}, \underline{p}_k^{n+1}\right)]_{ij} = [f_k^p]_{ij}\,, \tag{26}$$

$$[L_k^{c_s}\left(\underline{h}_k^{n+1}, \underline{p}_k^{n+1}, \underline{c_s}_k^{n+1}\right)]_{ij} = [f_k^{c_s}]_{ij}\,. \tag{27}$$

Given an estimate, $(\underline{h_0}_k^{n+1}, \underline{p_0}_k^{n+1}, \underline{c_{s0}}_k^{n+1})$, to the solution of this system, the smoother then defines the updates to this at node (i, j) to be the solution of the following 3×3 system (where all expressions are evaluated at the latest estimate):

$$\frac{\partial[L_k^h]_{ij}}{\partial(h_k)_{ij}}\Delta h + \frac{\partial[L_k^h]_{ij}}{\partial(p_k)_{ij}}\Delta p + \frac{\partial[L_k^h]_{ij}}{\partial(c_{s,k})_{ij}}\Delta c_s = [f_k^h]_{ij} - [L_k^h]_{ij}\,, \tag{28}$$

$$\frac{\partial[L_k^p]_{ij}}{\partial((h_k)_{ij}}\Delta h + \frac{\partial[L_k^p]_{ij}}{\partial(p_k)_{ij}}\Delta p + \frac{\partial[L_k^p]_{ij}}{\partial(c_{s,k})_{ij}}\Delta c_s = [f_k^p]_{ij} - [L_k^p]_{ij}\,, \tag{29}$$

$$\frac{\partial[L_k^{c_s}]_{ij}}{\partial(h_k)_{ij}}\Delta h + \frac{\partial[L_k^{c_s}]_{ij}}{\partial(p_k)_{ij}}\Delta p + \frac{\partial[L_k^{c_s}]_{ij}}{\partial(c_{s,k})_{ij}}\Delta c_s = [f_k^{c_s}]_{ij} - [L_k^{c_s}]_{ij}\,. \tag{30}$$

Hence the updated approximation to the solution at point (i, j) (on grid level k) is given by: $\widetilde{h_{0i,j}}^{n+1} = h_{0i,j}^{n+1} + \Delta h$, $\widetilde{p_{0i,j}}^{n+1} = p_{0i,j}^{n+1} + \Delta p$ and $\widetilde{c_{s,0i,j}}^{n+1} = c_{s,0i,j}^{n+1} + \Delta c_s$. Furthermore this 3×3 matrix problem that must be solved for each grid point is simplified by the fact $\frac{\partial[L_k^p]_{ij}}{\partial(c_{s,k})_{ij}} = 0$ since the discretised pressure equation, (26), does not explicitly depend on the solvent concentration. In all other respects the solution procedure used here is as described in Gaskell et al[10].

IV Results and discussion

Results for gravity-driven flow of continuous thin films with evaporation are presented in three complementary subsections: the simplest case of flow over substrates without topography is first studied analyti-

cally, before two-dimensional and three-dimensional flows over topography are investigated numerically. Unless otherwise stated, results are for a film with $H_0 = 70\mu m$, $\alpha = 30^o$ and the parameters listed in Table 1, with mesh independent numerical solutions obtained on a grid extending over 50 Capillary lengths ($\beta = 50$) in the X and Y directions using a finest grid level of 257×257 ($k_f = 8$).

A. Evaporating flow over a flat substrate

The problem of a pure liquid film draining down a flat, inclined plane for the case of constant flux is trivial in the absence of evaporation, yielding a liquid film of uniform thickness, the behaviour of which is modified when solvent evaporation induces viscosity variations. Intuition suggests that the free surface shape is determined by two competing effects as the fluid flows further and further downstream: thinning due to evaporative solvent loss and thickening due to the resultant increase in viscosity. By adopting the same assumptions as Huppert[22], who investigated the fingering instability in gravity-driven thin films down a slope, a simple analytical solution for the film thickness, solvent concentration and therefore the viscosity can be obtained; this also provides a useful means of validating corresponding numerical solutions. Huppert assumed that the effects of surface tension and the component of gravity normal to the substrate could be neglected, so that the fluid motion is dictated by a balance between the tangential component of gravity driving the liquid and viscous stresses, and derived a simple similarity solution which describes the evolution of the free surface as a function of time. In the absence of a topography, the free surface can only be deformed by the effects of evaporation which act on a sufficiently long wavelength for surface tension effects to be safely neglected.

While Huppert considered the evolution of a fixed amount of liquid located at time zero at the top of an inclined plane, a corresponding steady state analytic solution can be found for the present configuration in which the film is fed by a constant flux at inlet. Invoking Huppert's assumptions, equations (6) and (13) become:

$$-2\frac{d}{dx}\left[\frac{h^3}{3\tilde{\mu}}\right] - e = 0\,, \tag{31}$$

$$-2\frac{h^2}{3\tilde{\mu}}\frac{dc_s}{dx} + e\frac{(c_s-1)}{h} = 0\,, \tag{32}$$

where partial derivatives have been replaced by ordinary derivatives in this one-dimensional analysis. The first equation (31) simply yields

$$\frac{h^3}{3\tilde{\mu}} = -e\frac{x}{2} + K_1 \,, \tag{33}$$

while the upstream boundary conditions, $h(x=0) = \tilde{\mu}(x=0) = 1$, lead to $K_1 = 1/3$.

Combining equations (32) and (33) and imposing the condition $c_s(x=0) = c_0$, yields

$$c_s = \frac{\frac{2}{3}(1-c_0)}{ex - \frac{2}{3}} + 1 \,, \tag{34}$$

Equation (34) reveals that at $x_0 = \frac{2}{3}\frac{c_0}{e}$ ($X_0 = \frac{Q_0 c_0}{E}$ in dimensional quantities) $c_s = 0$, indicating that the solvent has evaporated completely there, a result that simply asserts the conservation of solvent since $Q_0 c_0$ is the inlet flux of solvent and EX_0 is the amount of solvent lost through evaporation. Equations (1) and (34) enable the viscosity derivative to be rewritten as

$$\frac{d\tilde{\mu}}{dx} = -a\tilde{\mu}\frac{dc_s}{dx} = a\tilde{\mu}e\frac{2\,(1-c_0)}{3\left(ex - \frac{2}{3}\right)^2} \,, \tag{35}$$

so that differentiation of eq. (33) yields

$$-2\frac{h^2}{e\tilde{\mu}}\left(ex - \frac{2}{3}\right)^2 \frac{dh}{dx} = \left(ex - \frac{2}{3}\right)\left(ex - \frac{2}{3}\,(1 - a\,(1-c_0))\right) \,. \tag{36}$$

The factor multiplying the film thickness derivative in equation (36) is necessarily negative and therefore the sign of the film thickness derivative is dictated by the sign of the quadratic function on the right-hand side. One of its roots, $x_1 = \frac{2}{3e}$, can be disregarded since it lies beyond x_0, the location at which all solvent has evaporated. Depending on the value of the second root, $x_2 = \frac{2}{3e}\,(1 - a\,(1-c_0))$, three different types of free surface shape can be expected. If $x_2 \leq 0$, the surface rises because of the increase of viscosity as solvent evaporates; if $x_2 \geq x_0$, the film thickness monotonically decreases due to solvent loss by evaporation; in the intermediate case, where $0 < x_2 < x_0$, the film thins up to $x = x_2$ and then thickens for the reasons stated above. These three forms of free surface behaviour are illustrated in Figure 2. The values of x_2 and x_0, as per the figure, confirm that the behaviour of the free surface is dictated by the value of the x_2 root. Note that for very large values of a, the dramatic increases in both viscosity and film thickness due to solvent evaporation would quickly stop the flow.

Analytical solutions for the case with $e = 0.05$, $c_0 = 0.7$ and, following Schwartz et al[9], $a = 70$ are compared with corresponding numerical results in Figure 3. An additional (x^+, y^+) coordinate system is introduced for the presentation of results. This has the same origin as the (x, y) coordinate system but the norm of the unit vector is the Capillary length, i.e. $(x^+, y^+) = \beta(x, y)$ where $L = \beta L_d$. Figure 3 shows the profiles of film thickness, solvent concentration and viscosity obtained at different dimensionless times ($t = 1$, $t = 2$ and $t = 4$) and demonstrates that, after a transient initial stage, the film reaches a steady-state; indeed, from $t = 2$, onwards, the time-dependent simulation is almost indistinguishable from the steady-state analytical solution. This good agreement between numerical and analytical solutions indicates that, in this regime, the effects of the surface tension and hydrostatic pressure included in the numerical simulations, but neglected in the analytical model, are indeed negligible.

B. Evaporating flow over a spanwise topography

Flows over one-dimensional topography in the absence of evaporation have been widely studied. That over a step-up topography, for example, is known to produce a free surface depression[1] just upstream of the topography, while flow over a step-down creates a Capillary ridge[2] before relaxation of the free surface further downstream. Of particular interest here is examining the validity of previous studies of evaporative flow during industrial spin coating[17,19,31], which have assumed that the free surface profile can be predicted by dividing the process into two stages. In the first, flow-dominated stage, the film profile is considered to be controlled by a balance between a driving force and the capillary force within the lubrication approximation, under the assumption that neither the topography nor the free surface disturbance caused by it affect the distribution of solvent within the resin/solvent mixture. In the second, or shrinkage, stage the film simply shrinks without flow by further evaporative drying. The transition between the two stages if often assumed to occur abruptly at a critical solvent concentration[17,19].

The flow over a step-up topography is considered first. Full-width topographies are defined by means of a cubic function, bridging two regions of the substrate of different heights, as follows[29]:

$$s(x) \;=\; 0 \quad \text{for} \quad x < x_t - \frac{\gamma}{2}\,,$$

$$
\begin{aligned}
s(x) &= s_0 \left[-2 \left(\frac{x-(x_t-\frac{\gamma}{2})}{\gamma} \right)^3 + 3 \left(\frac{x-(x_t-\frac{\gamma}{2})}{\gamma} \right)^2 \right] \\
&\qquad \text{for} \quad x_t - \frac{\gamma}{2} < x < x_t + \frac{\gamma}{2} \,, \\
s(x) &= s_0 \quad \text{for} \quad x > x_t + \frac{\gamma}{2} \,, \qquad (37)
\end{aligned}
$$

where γ controls the steepness of the topography. The form of equation (37) ensures that the substrate function, $s(x)$, is never multivalued and approximates sharp edges in the limit of $\gamma \to 0$. As written it defines a step-up while a similar expression exists for a step-down; the trench considered later is simply defined as a combination of the two.

Figure 4 shows numerical predictions of the free surface profile for flows with $0 \leq e \leq 0.05$ over a step height of $s_0 = 0.5$ (half the asymptotic film thickness) with $\gamma = 0.05$; the corresponding topography profile is also shown. As expected, increasing the solvent evaporation rate increases the viscosity of the resin/solvent mixture and leads to an increase in the film thickness as the mixture flows further downstream. The downstream viscosity increase for the $e = 0.05$ case is also shown in Figure 4, as is the resin/solvent interface defined by $h_r + s$, where $h_r = (1 - c_s)h$. The latter is fictitious, of course, since the resin and solvent are assumed to be well-mixed. However, despite the obvious increase in film thickness with solvent evaporation rate, the free surface profiles near the step-up are qualitatively similar, with progressively smaller free surface depressions as the evaporation rate increases.

Figure 5 compares numerical predictions for evaporating flow over the topography of Figure 4 with the analytical solution for the particular case of $e = 0.05$. Although the analytical solution cannot be expected to be valid near the topography, any significant differences between the two predictions would indicate that the topography is having a lasting influence on the composition of the resin/solvent mixture. This finding would contradict the assumptions of the earlier analyses of evaporating, spin coating flows cited above[17,19]. In fact, the steady-state one-dimensional form of the governing equations (9) and (13)

$$
\begin{aligned}
\frac{d}{dx} \left[\frac{h^3}{3\tilde{\mu}} \left(\frac{dp}{dx} - 2 \right) \right] - e &= 0 \,, \qquad (38) \\
\frac{h^2}{3\tilde{\mu}} \left(\frac{dp}{dx} - 2 \right) \frac{dc_s}{dx} + e \frac{(c_s - 1)}{h} &= 0 \,, \qquad (39)
\end{aligned}
$$

are of the same form as equations (31) and (32) developed from Huppert's analysis but with the inclusion

of the $\left(\frac{dP}{dX}-2\right)$ terms. Eliminating $\frac{h^3}{3\tilde{\mu}}\left(\frac{dp}{dx}-2\right)$ from equations (38) and (39) yields the following ordinary differential equation for c_s:

$$\left(ex-\frac{2}{3}\right)\frac{dc_s}{dx}+e(c_s-1)=0. \tag{40}$$

The solution of this equation which satisfies the condition $c_s=0$ at $x=0$ is exactly the same as that found earlier using Huppert's assumptions, i.e. equation (34). Hence spanwise topography can have no influence on the solvent concentration for the uniform evaporation rates considered here, while the film thickness and pressure are affected by the exponent a in the viscosity law (1). Figure 5 confirms the independence of solvent concentration from the topography and shows that the free surface disturbances caused by the topography are quickly dissipated further downstream.

The next three Figures consider gravity-driven, evaporating flow over a spanwise trench-shaped topography whose lateral extent is two Capillary lengths and with a depth of $0.7H_0$, i.e. $s_0=-0.7$. Figure 6 shows the profile of the topography, together with the computed free surface, fictitious resin/solvent interface and viscosity ratio profiles for the case $e=0.05$, $a=70$ and $c_0=0.7$. The free surface shows the same features as observed in the non-evaporating case[1,11], namely a Capillary ridge followed by a depression over the trench shifted vertically, of course, due to the increasing viscosity in the downstream direction as a consequence of evaporative solvent loss. Figure 7 compares the numerical solution given in Figure 6 with the analytical solution for the case without any topography. Once again, the agreement is excellent with free surface disturbances near the (large) topography quickly dissipating downstream of it.

Flow over this trench-shaped topography is now studied for a second, much larger evaporation rate ($e=0.4$) in order to assess the effect of a greater streamwise variation in the solvent concentration. In Figure 8, the parameter $a=2$ has been chosen so that $0<x_2=0.667<x_0=1.167$ with the result that the analysis predicts that the film will thin up to $x=x_2$ and then thicken thereafter. The free surface exhibits the expected features of a Capillary ridge just upstream of the trench and a depression over it and, for this higher evaporation rate, the numerical predictions agree well with the corresponding analytical ones. In particular, the analytical prediction that the dip in the free surface will be at $x^+{}_2=\beta x_2=33.35$, agrees well with that predicted numerically, even when the flow is over the large trench shown in Figure 6.

In summary, the assumption of earlier spin coating studies[17,19,31] that spanwise topography has no effect on the composition of the resin/solvent mixture has been found to be valid for the two-dimensional flows

studied here.

C. Evaporating flow over a localised topography

The topography considered is a square trench of extent 5 Capillary lengths ($l_t = w_t = 0.1$ since the computational domain is $50L_d \times 50L_d$) with a depth equal to half the asymptotic film thickness, $s_0 = -0.5$, centred at $(x_t^+, y_t^+) = (17.5, 25.0)$. The topography $s(x,y)$ is given by

$$s(x,y) = \frac{s_0}{b_0}\left(tan^{-1}\left(\frac{x^+ - x_t^+ - l_t/2}{l_t\gamma}\right) + tan^{-1}\left(\frac{-x^+ + x_t^+ - l_t/2}{l_t\gamma}\right)\right) \times \left(tan^{-1}\left(\frac{y^+ - y_t^+ - w_t/2}{l_t\gamma}\right) + tan^{-1}\left(\frac{-y^+ + y_t^+ - w_t/2}{l_t\gamma}\right)\right), \quad (41)$$

where

$$b_0 \;=\; 4\tan^{-1}\left(\frac{1}{2\gamma}\right)\tan^{-1}\left(\frac{w_t/l_t}{2\gamma}\right). \quad (42)$$

For consistency with earlier results, the topography steepness parameter, γ, is once again set equal to 0.05.

Numerical results, after reaching steady-state, are shown in Figure 9 for $e = 0.0$ and $e = 0.01$. The free surface for the evaporating case ((c)) displays similar features to its non-evaporating counterpart[11] (9(a)): an upstream Capillary ridge with comet tails on each side of the topography and a downstream surge in the middle. The pressure field for the evaporating case (9(d)) is also similar to its non-evaporating counterpart (9(b)) with two steep peaks formed on the upstream and downstream walls of the topography separated by a pressure drop across it. The solvent concentration field is shown in Figure 9(e). As well as the inevitable solvent depletion in the downstream direction caused by evaporation, in contrast with two-dimensional flows the localised topography produces a localised disturbance to the solvent concentration field which persists in the downstream direction. The corresponding viscosity field is shown in Figure 9(f). Due to the chosen viscosity dependence on solvent concentration, equation (1), peaks in solvent concentration correspond to viscosity minima and vice versa.

Given the general lack of experimental data available for thin film evaporating flows a plausible explanation for the spanwise variation in the solvent concentration observed in the presence of localised topography is as follows. As fluid flows over the trench, at all spanwise locations, y, an equal amount of

solvent will be lost through evaporation at a fixed streamwise location, x. Now, since the fluid layer covering the trench is deeper than elsewhere, the resulting decrease in solvent concentration will be smallest there; consequently, the solvent concentration immediately downstream of the topography will be greater than its surroundings. This argument is consistent with the last term in equation (13) which tends to decrease the rate of change of solvent concentration where the film thickness increases and vice versa. The localised downstream 'surge' out of the trench[11] arises similarly from a corresponding mass continuity consideration.

The above features are seen more clearly by considering spanwise profiles downstream of the topography. Figure 10 shows the spanwise variation ($0 \leq y^+ \leq 50$) in film thickness, pressure, solvent concentration and viscosity at three different spanwise locations: $x^+ = 25$, 30 and 35. The amplitudes of the film thickness and pressure variations shown in Figures 10(a) and (b) clearly decay in the downstream direction, together with an accompanying shift of the extrema in h and p away from the streamwise centreline, $y^+ = 25$. The latter leads to the characteristic "horseshoe" shape of the Capillary wave. In contrast, Figures 10 (c) and (d), the peak and troughs in the spanwise solvent concentration (and hence viscosity) caused by the streamwise topography walls persist in the downstream direction. The heterogeneity in solvent, and hence functional resin, concentration triggered by this relatively simple three-dimensional topography may have undesirable consequences on the quality of the remaining dried film. Clearly, if all the solvent evaporated instantaneously, these variations in resin concentration would appear as defects in the dried film downstream of the topography. The prediction of the final dried film profile is essential from an industrial viewpoint and constitutes a natural extension to the present work.

Decré and Baret[1] and Gaskell et al[11] found that for the non-evaporating case the free surface responds to small topographies ($|s_0| \leq 0.1$) in a near-linear fashion. The final figure considers the linearity issue for evaporating flows. Figure 11(a) shows the surface constructed by averaging the free surface for the flow over the trench topography in Figure 9 with that over an equal but opposite topographic peak with $s_0 = 0.5$. Although the two surfaces largely cancel one another out to leave the expected approximately uniform increase in free surface height with downstream location due to solvent depletion, as reported in the non-evaporating case[11], there are small differences in and around the topography and in the positions of the spanwise extrema. Note, however, that these differences are small compared to the free surface disturbances caused by the topographies in isolation. Figure 11(b) compares the streamwise free surface

profiles through the centre of the topography, $y^+ = 25$. This shows clearly that the average profile is indeed close to that predicted for the same evaporation rate but without a topography, i.e. $s_0 = 0$. Even for flow past large topographies with $s_0 = \pm 0.5$, for which the lubrication assumptions are not strictly valid, the maximum difference between the two profiles is less than 2%. Table 2 presents further data on the validity, or otherwise, of Decré and Baret's assumption of a linear free surface response to topography. It shows that, as expected, its accuracy increases rapidly as topography amplitude is reduced and that increasing evaporation rate also has the same effect but to a lesser degree.

VI Conclusion

The flow of an evaporating thin liquid film down an inclined plane has been explored in the framework of the lubrication and *well-mixed* approximations, analytically in the case of flat substrates and numerically for flows past well defined topography.

The analytical solution to the simplified problem, when the effect of surface tension and hydrostatic pressure can be neglected, provides a convenient test case. For the viscosity dependence upon solvent concentration used here, equation (1), three regimes of free surface development are identified depending on the value of $x_2 = \frac{2}{3e}(1 - a(1 - c_0))$ ($X_2 = \frac{Q_0}{E}(1 - a(1 - c_0))$ in dimensional quantities). In the first regime, the viscosity increase caused by solvent depletion in the downstream direction causes the film to thicken monotonically while in the second the opposite behaviour is observed: the film simply thins monotonically due to solvent loss. In the final regime the delicate balance between solvent loss and its associated viscosity increase causes the film to thin initially before thickening further downstream when the viscosity increase becomes dominant.

For two-dimensional evaporating flows over spanwise topography, the analysis predicts that solvent concentration cannot be affected by the presence of the topography and depends only on the evaporation rate and the initial solvent concentration; film thickness and pressure do, however, depend on the particular viscosity law used. Numerical predictions for two-dimensional evaporating flows over a range of spanwise topographies are found to agree well with analytical predictions and, further, to support the assumptions of previous studies of spin coating[17,19,31] that in the flow-dominated stage the presence of topography

has no effect on the composition of the resin/solvent mixture. In contrast, however, the presence of a localised topography such as a peak or trench can lead to persistent heterogeneities in the composition of the resin/solvent mixture. In the cases studied here, flows over square trenches and peaks, the sides of the topography can cause large local extrema in solvent concentration which could lead to unacceptable variations in the properties of the dry, functional coating. Clearly, the ability to predict the interactions between evaporating flows and localised topography will be of significant benefit to scientists and industrialists alike.

Acknowledgement

The authors are grateful to Philips Electronics, Eindhoven, for sponsoring this work and to Yeaw-Chu Lee for his helpful discussions on Multigrid methods.

References

[1] M.M.J. Decré, and J-C. Baret, "Gravity driven flows of viscous liquids over two-dimensional topographies," J. Fluid Mech. **487**, 147 (2003).

[2] S. Kalliadasis, C. Bielarz, and G.M. Homsy, "Steady free-surface thin film flow over two-dimensional topography," Phys. Fluids **12**, 2845 (2000).

[3] S. Kalliadasis, and G.M. Homsy, "Stability of free surface thin-film flows over topography," J. Fluid Mech. **448**, 387 (2001).

[4] A. Mazouchi, and G.M. Homsy, "Free surface Stokes flow over topography," Phys. Fluids **13**, 2751 (2001).

[5] C. Bielarz, and S. Kalliadasis, "Time-dependent free-surface thin film flows over topography," Phys. Fluids **15**, 2512 (2003).

[6] C.M. Gramlich, A. Mazouchi, and G.M. Homsy, "Time-dependent free surface Stokes flow with a moving contact line. II. Flow over wedges and trenches," Phys. Fluids **16**, 1660 (2004).

[7] M. Hayes, S.B.G. O'Brien, and J.H. Lammers, "Green's function of steady flow over a two-dimensional topography," Phys. Fluids **12**, 2845 (2000).

[8] L.W. Schwartz, and R.R. Eley, "Simulation of droplet motion on low energy and heterogeneous surfaces," J. Colloid Interface Sci. **202**, 173 (1998).

[9] L.W. Schwartz, R.V. Roy, R.R. Eley, and S. Petrash, "Dewetting patterns in a drying liquid film," J. Colloid Interface Sci. **234**, 363 (2001).

[10] P.H. Gaskell, P.K. Jimack, M. Sellier, and H.M. Thompson, "Efficient and accurate time adaptive multigrid simulations of droplet spreading," Int. J. Numer. Meth. Fluids **45**, 1161 (2004).

[11] P.H. Gaskell, P.K. Jimack, M. Sellier, H.M. Thompson, and M.C.T. Wilson, "Gravity-driven flow of continuous thin liquid films on non-porous substrates with topography," J. Fluid Mech. **509**, 253 (2004).

[12] W.S. Overdiep, "The levelling of paints," Prog. Org. Coat. **14**, 159 (1986).

[13] M.H. Eres, D.E. Weidner, and L.W. Schwartz, "Three dimensional direct numerical simulation of surface-tension-gradient effects on the leveling of an evaporating multicomponent fluid," Langmuir **15**, 1859 (1999).

[14] D.E. Weidner, L.W. Schwartz, and R.R. Eley, "Role of surface tension gradients in correcting coating defects in corners," J. Colloid Interface Sci. **179**, 66 (1996).

[15] P.L. Evans, L.W. Schwartz, and R.V. Roy, "A mathematical model for crater defect formation in drying paint layer," J. Colloid Interface Sci. **227**, 191 (2000).

[16] V.S. Ajaev, "Viscous flow of a volatile liquid on an inclined heated surface," J. Colloid Interface Sci. **280**, 165 (2004).

[17] D. Meyerhofer, "Characteristics of resist films produced by spinning," J. Appl. Phys. **49**, 3993 (1978).

[18] D.E. Bornside, C.W. Macosko, and L.E. Scriven, "Spin coating - one-dimensional model," J. Appl. Phys. **66**, 5185 (1989).

[19] L.E. Stillwagon, and R.G. Larson, “Leveling of thin films over uneven substrates during spin coating,” Phys. Fluids **2**, 1937 (1990).

[20] L.M. Puerrung and B.G. Graves, “Film thickness profiles over topography in spin coating,” J. Electrochem. Soc. **138**, 2115 (1991).

[21] L.M. Puerrung and B.G. Graves, “Spin coating over topography,” IEEE Trans. Semi. Man. **6**, 72 (1993).

[22] H.E. Huppert, “Flow and instability of a viscous current down a slope,” Nature **300**, 427 (1982).

[23] A. Oron, S.H. Davis, and S.G. Bankoff, “Long-scale evolution of thin liquid films,” Rev. Mod. Phys. **69**, 931 (1997).

[24] A.L. Bertozzi, and M.P. Brenner, “Linear stability and transient growth in driven contact lines,” Phys. Fluids **9**, 530 (1997).

[25] S.D. Howison, J.A. Moriarty, J.R. Ockendon, and E.L. Terril, “A mathematical model for drying paint layer,” J. Eng. Math. **32**, 377 (1997).

[26] B.W. Van de Fliert, “A free boundary problem for evaporating layers,” Nonlinear Anal.-Theo. **47**, 1785 (2001).

[27] A. Brandt, “ Multi-level adaptive solutions to boundary-value problems,” Math. Comput. **31**, 333 (1977).

[28] A. Brandt, “Guide to multigrid development,” In: *Multigrid methods: lecture notes in mathematics,* edited by W. Hackbush and U. Trottenberg (Springer-Verlag, Berlin, 1982), p. 220.

[29] M. Sellier, PhD thesis, University of Leeds, U.K (2003).

[30] U. Trottenberg, C. Oosterlee, and A. Schueller, *Multigrid* (Academic Press, London, 2001).

[31] C.J. Lawrence, “The mechanics of spin coating of polymer films,” Phys. Fluids **31**, 2786 (1988).

Scalings, dimensionless groups	Equation	Value in computations	Min value	Max value
Q_0	$Q_0 = \frac{{H_0}^3 \rho g \sin\alpha}{3\mu_0}$	$2.3 \times 10^{-8}\mathrm{m}^2\mathrm{s}^{-1}$	1.12×10^{-9}	5.6×10^{-7}
U_0	$U_0 = \frac{3Q_0}{2H_0}$	4.9×10^{-4} ms^{-1}	2.4×10^{-5}	0.012
L_d	$L_d = \left(\frac{\sigma H_0}{3\rho g \sin\alpha}\right)^{1/3}$	5.5×10^{-4} m	4.57×10^{-4}	6.2×10^{-4}
L	$L = \beta L_d$	2.7×10^{-2}m	0.02285	0.031
ε	$\varepsilon = \frac{H_0}{L}$	2.5×10^{-3}	0.0023	0.0031
Ca	$Ca = \frac{\mu_0 U_0}{\sigma}$	3.5×10^{-4}	2.4×10^{-4}	6×10^{-4}
N	$N = Ca^{1/3}\cot\alpha$	1.2×10^{-1}	0.108	0.146
e	$e = \frac{E}{\varepsilon U_0}$	8×10^{-3} - 8×10^{-1}	2.69×10^{-4}	18.116
d	$d = \frac{D}{LU_0}$	7.4×10^{-4}	2.688×10^{-6}	0.182

TABLE 1: The value of scalings and dimensionless groups for the flow of a 70 μm thick film down a plane inclined at 30^o to the horizontal.

$\lvert s_0 \rvert$	$e = 0.0$	$e = 0.01$	$e = 0.05$
0.1	0.07	0.06	0.05
0.25	0.45	0.40	0.32
0.5	1.80	1.56	1.25

TABLE 2: Effect of topography amplitude, $|s_0|$, and evaporation rate, e on the validity of Decré and Baret's linearity assumption. Comparison between thickness profiles obtained (a) by superposing solutions for equal and opposite topographies (41) and (b) the corresponding flow in the absence of topography, i.e. $s_0 = 0$. Percentage differences along the streamwise topography centreline, $y^+ = 25$, are given.

Figure Captions

Figure 1: Schematic diagram of a three-dimensional thin film flowing over a substrate inclined at angle α to the horizontal with a three-dimensional protrusion ($S_0 > 0$) and a three-dimensional depression ($S_0 < 0$), showing the coordinate system used. Defining parameters for the protrusion are given.

Figure 2: Theoretical streamwise profiles of film thickness (full line) and solvent concentration (dashed line) for a gravity-driven film on a flat substrate for the parameters shown.

Figure 3: Comparison of the streamwise profiles of film thickness, h, solvent concentration, c_s, and viscosity ratio, μ/μ_0, obtained numerically at $t = 1$, $t = 2$ and $t = 4$ and analytically for a gravity-driven film on a flat substrate with $e = 0.05$, $c_0 = 0.7$ and $a = 70$.

Figure 4: Streamwise free surface profiles, $h+s$, for evaporating flow over a step-up topography, $s_0 = 0.5$, at $x^+ = 25$ with e =0, 0.01, 0.03 and 0.05, $c_0 = 0.7$ and $a = 70$. Also shown are the viscosity ratio, μ/μ_0, and fictitious resin solvent interface, h_r+s profiles for the $e = 0.05$ case.

Figure 5: Comparison between steady-state streamwise profiles of film thickness, h, solvent concentration, c_s, and viscosity ratio, μ/μ_0, obtained numerically and analytically for a gravity-driven film over a step-up topography with $e = 0.05$, $a = 70$ and $c_0 = 0.7$.

Figure 6: Streamwise profile of the free surface, $h+s$, the "resin/solvent interface", h_r+s, the topography, s, and the viscosity ratio, μ/μ_0, for the flow over a trench with $e = 0.05$, $s_0 = -0.7$, $a = 70$ and $c_0 = 0.7$.

Figure 7: Comparison of the steady-state streamwise profiles of the free surface, $h+s$, solvent concentration, c_s and viscosity ratio, μ/μ_0, obtained numerically and analytically for a gravity-driven film over a trench with $e = 0.05$, $s_0 = -0.7$, $a = 70$ and $c_0 = 0.7$.

Figure 8: Comparison of the steady-state streamwise profiles of the free surface, $h+s$, solvent concentration, c_s, and viscosity ratio, μ/μ_0, obtained numerically and analytically for a gravity-driven film over a trench with $e = 0.4$, $s_0 = -0.7$, $a = 2$ and $c_0 = 0.7$.

Figure 9: Three-dimensional surface plots for gravity-driven flow over a square trench topography with $s_0 = -0.5$, showing: (a) free surface, $h+s$, for $e = 0.0$ (b) pressure, p, for $e = 0.0$ (c) free surface, $h+s$,

for $e = 0.01$ (d) pressure, p, for $e = 0.01$ (e) concentration, c_s, for $e = 0.01$ and (f) viscosity ratio, μ/μ_0, for $e = 0.01$. Direction of flow indicated by arrows.

Figure 10: Spanwise profiles of (a) film thickness, h, (b) pressure, p, (c) solvent concentration, c_s, and (d) viscosity ratio, μ/μ_0, at 5, 10 and 15 capillary lengths downstream of the topography ($x^+ = 25$, 30 and 35 respectively) for the flow over a square trench topography with $s_0 = -0.5$, $e = 0.01$.

Figure 11: Superposition of solutions for flow over a square topography with $e = 0.01$ and $s_0 = \pm 0.5$. (a) Three dimensional plot of average free surface, (b) free surface profiles along the streamwise centreline, $y = 0.5$.

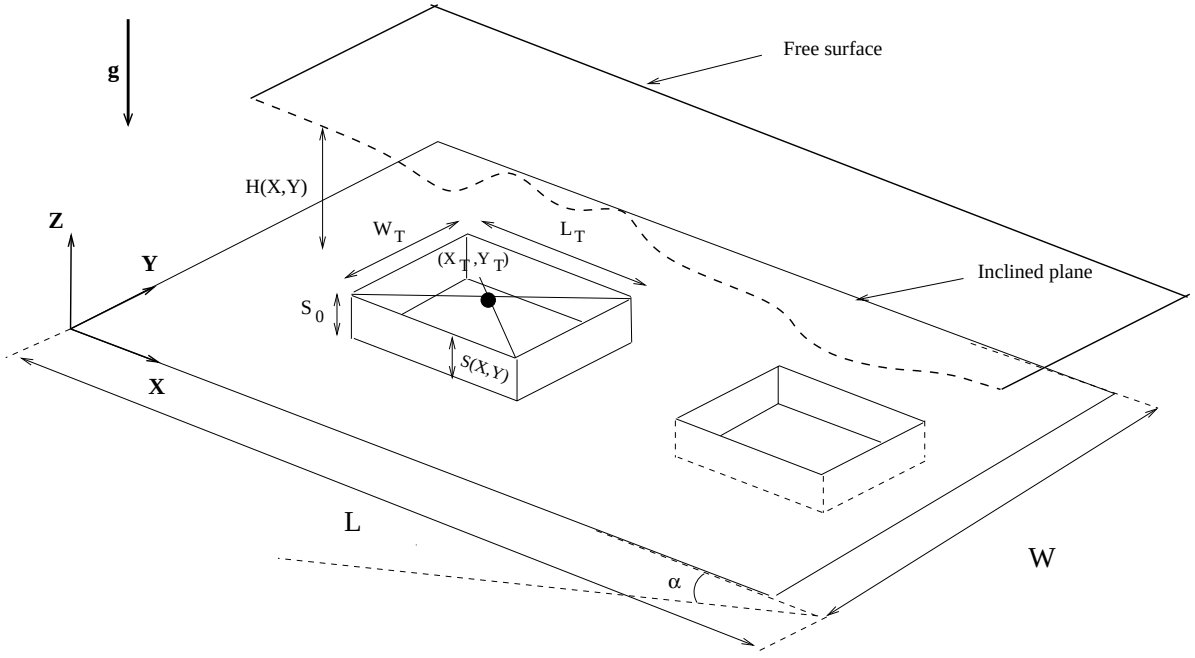
g
Free surface
H(X,Y)
Z
Y
X
W_T
L_T
(X_T,Y_T)
S_0
s(X,Y)
Inclined plane
L
W
α

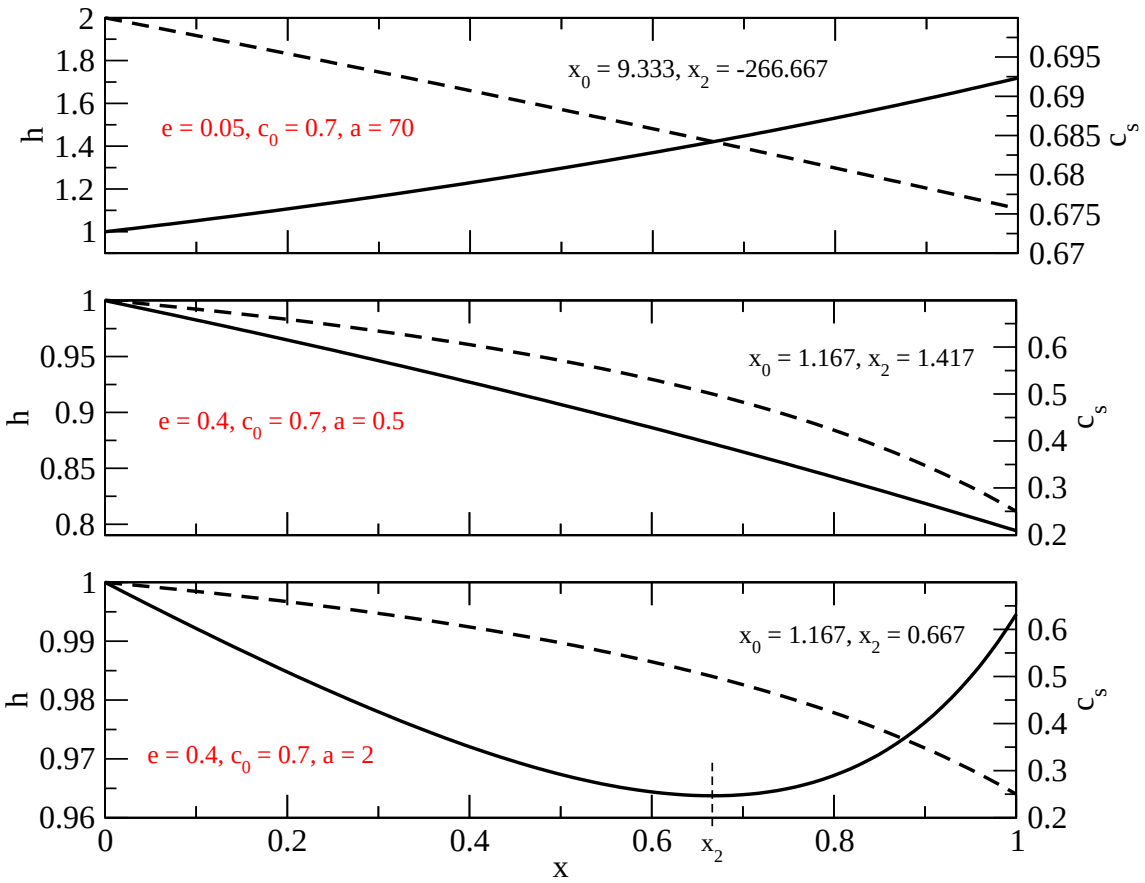
h
c_s
x_0 = 9.333, x_2 = -266.667
e = 0.05, c_0 = 0.7, a = 70
x_0 = 1.167, x_2 = 1.417
e = 0.4, c_0 = 0.7, a = 0.5
x_0 = 1.167, x_2 = 0.667
e = 0.4, c_0 = 0.7, a = 2
x
x_2

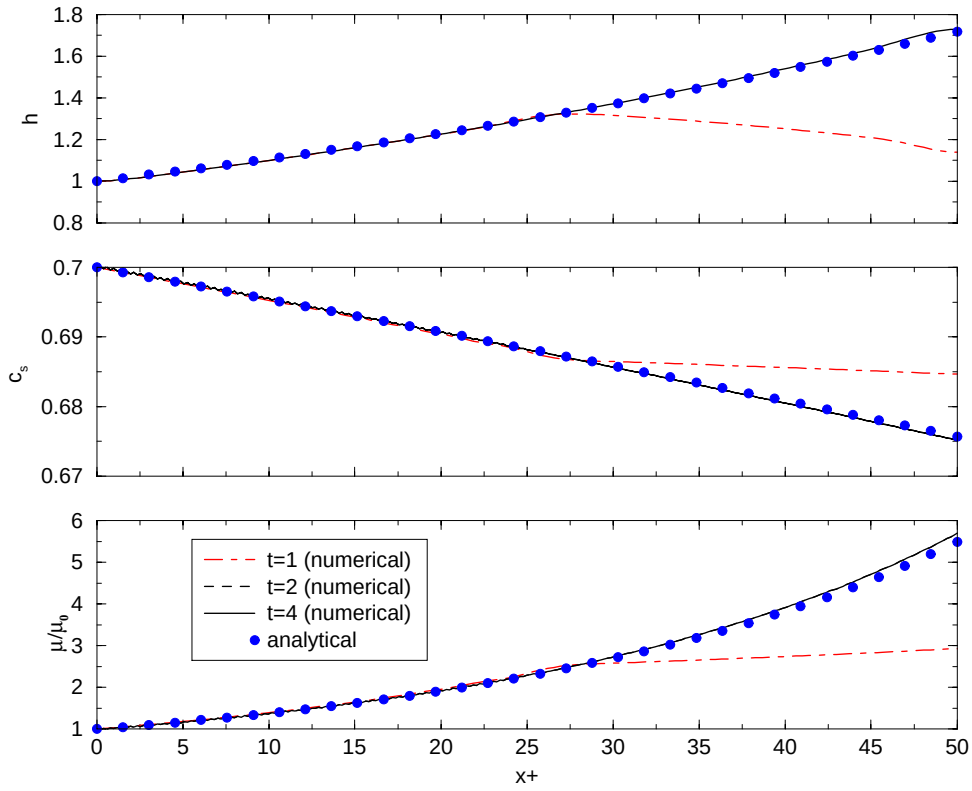
h
c_s
μ/μ_0
x+
t=1 (numerical)
t=2 (numerical)
t=4 (numerical)
analytical

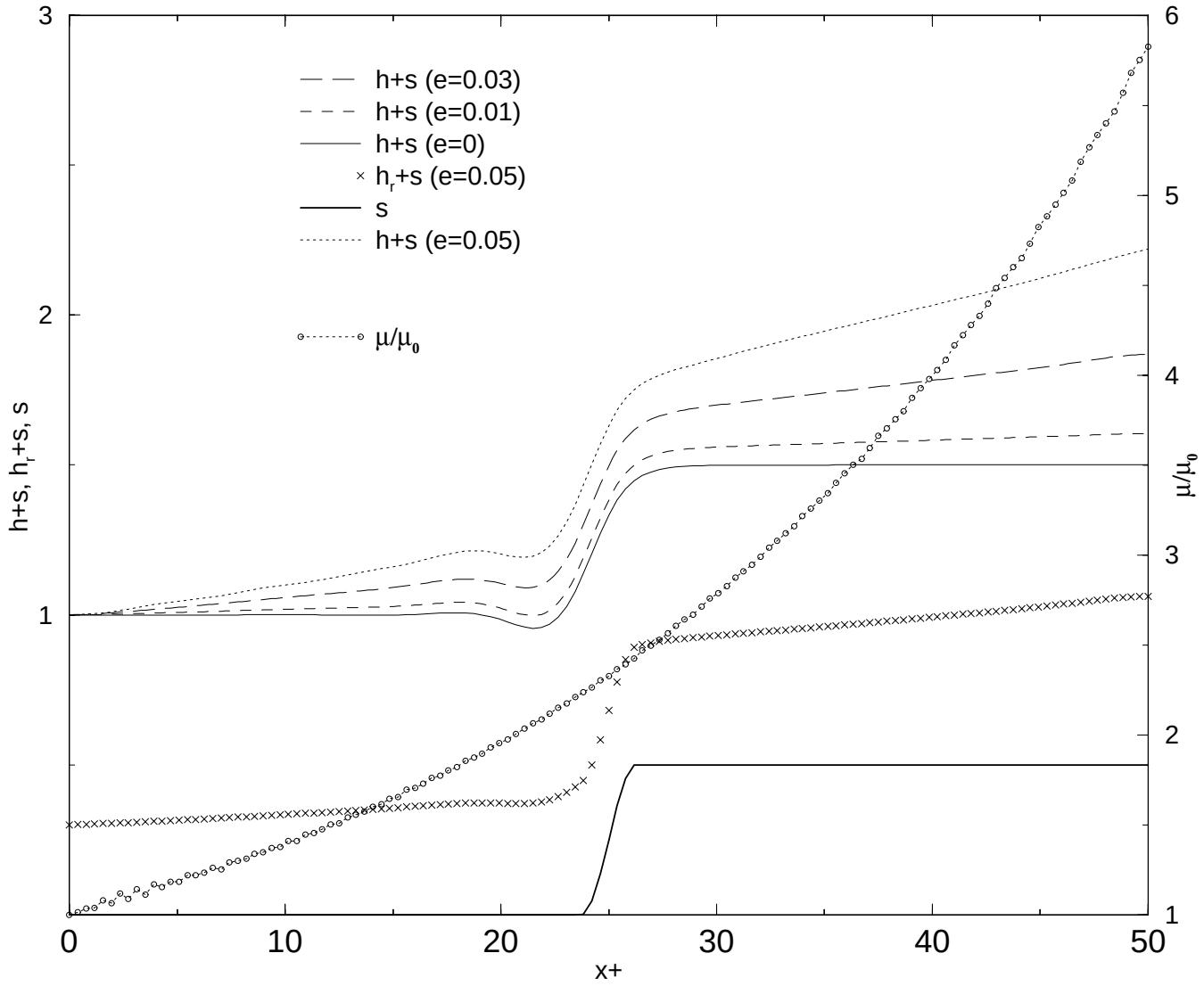
h+s (e=0.03)
h+s (e=0.01)
h+s (e=0)
h_r+s (e=0.05)
s
h+s (e=0.05)
μ/μ_0
h+s, h_r+s, s
μ/μ_0
x+
0
10
20
30
40
50
1
2
3
4
5
6

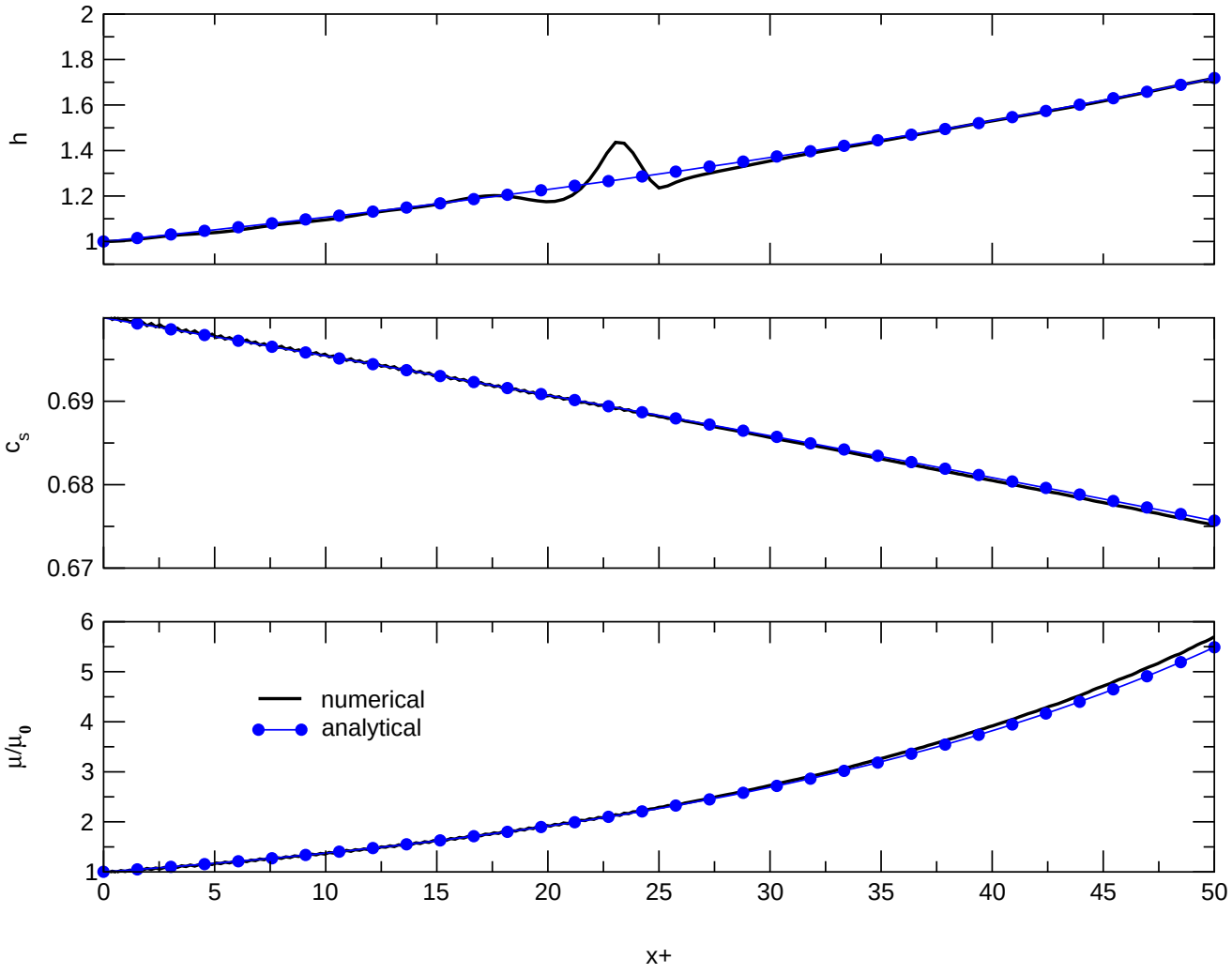
h
2
1.8
1.6
1.4
1.2
1
c_s
0.69
0.68
0.67
μ/μ_0
6
5
4
3
2
1
numerical
analytical
0
5
10
15
20
25
30
35
40
45
50
x+

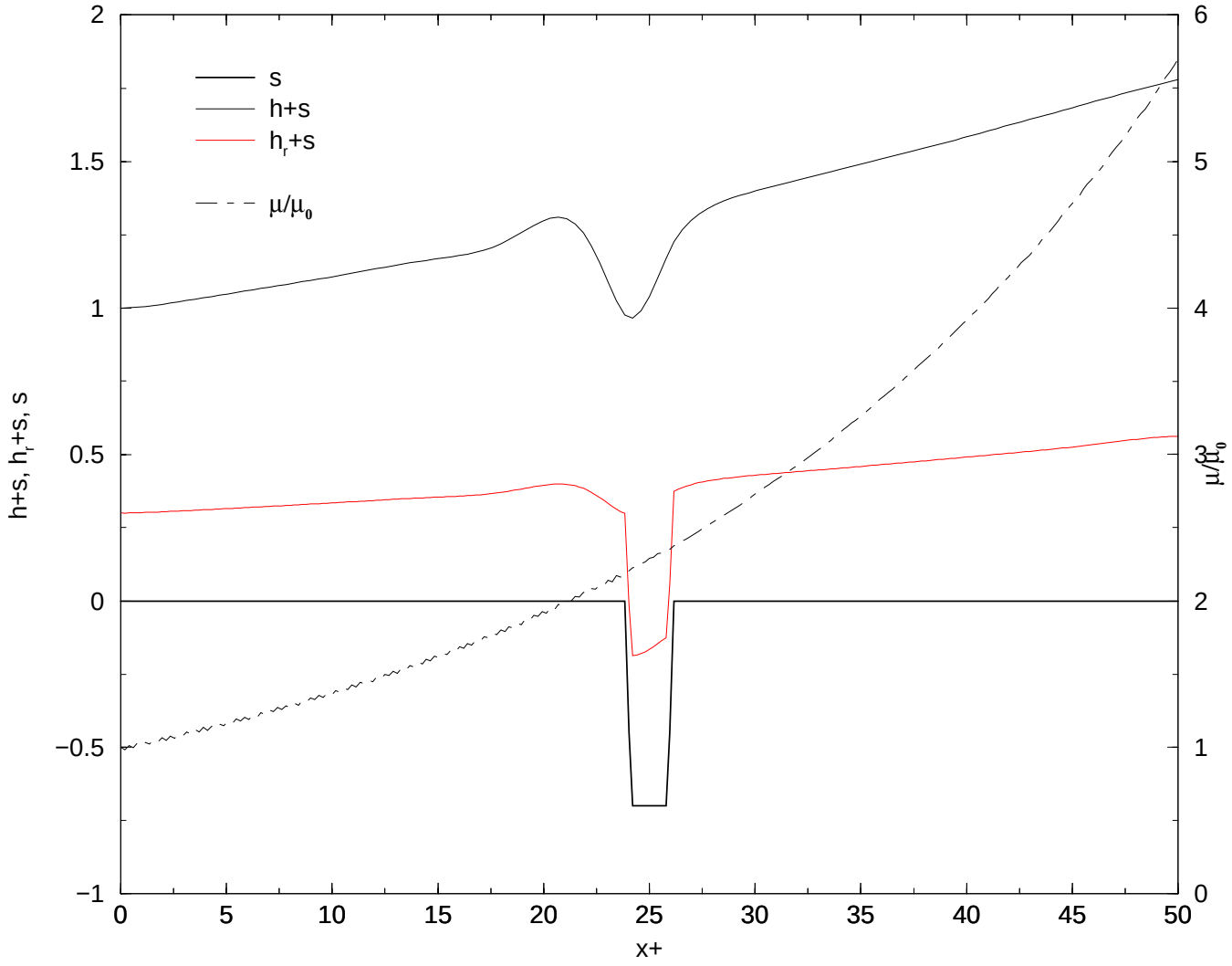
s
h+s
h_r+s
μ/μ_0
h+s, h_r+s, s
μ/μ_0
x+
2
1.5
1
0.5
0
−0.5
−1
6
5
4
3
2
1
0
0
5
10
15
20
25
30
35
40
45
50

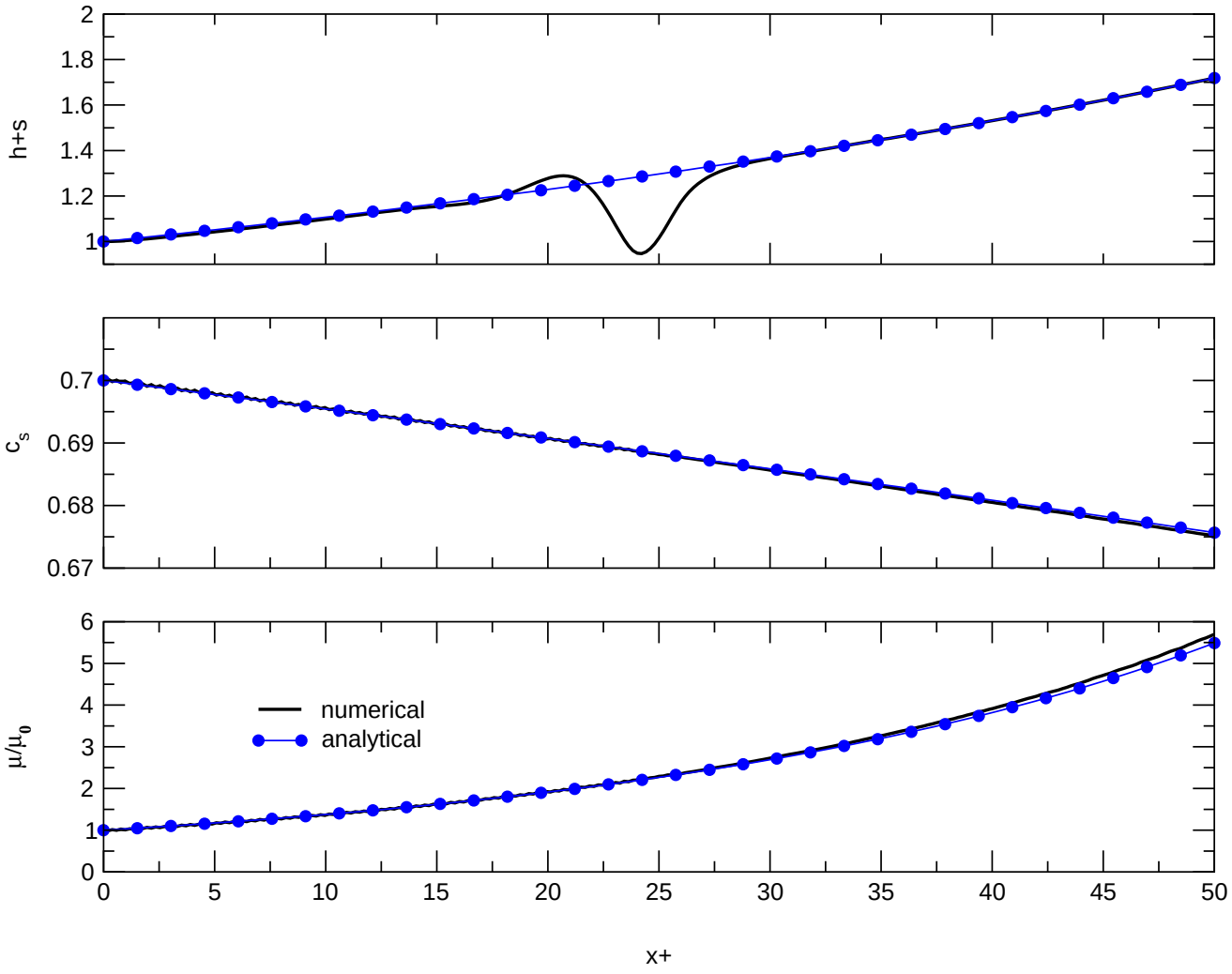
h+s
2
1.8
1.6
1.4
1.2
1
c_s
0.7
0.69
0.68
0.67
μ/μ_0
6
5
4
3
2
1
0
numerical
analytical
0
5
10
15
20
25
30
35
40
45
50
x+

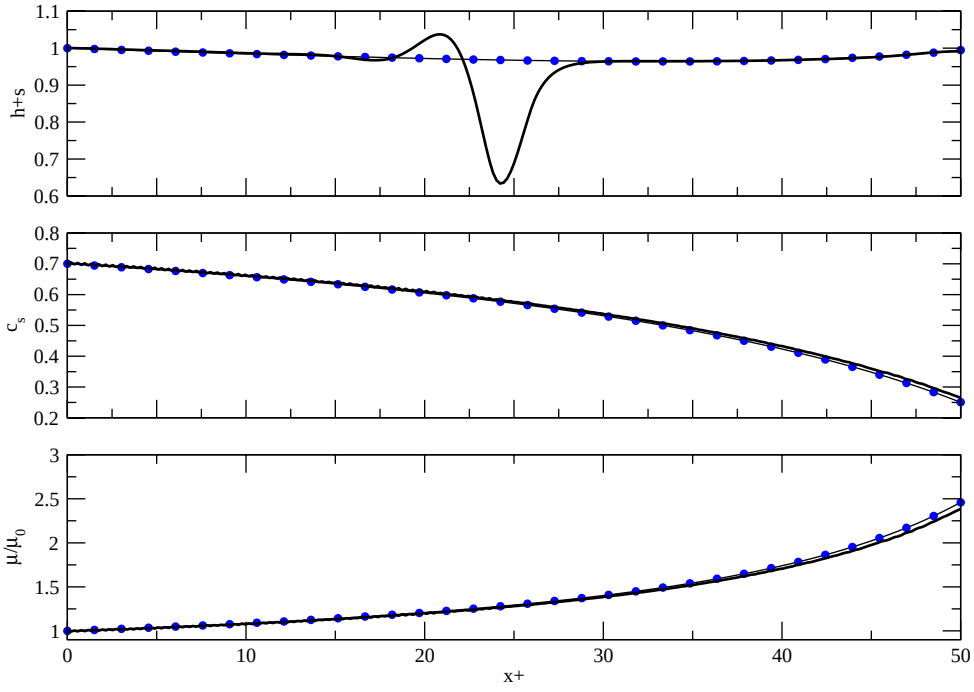
h+s
c_s
μ/μ_0
x+
0
10
20
30
40
50

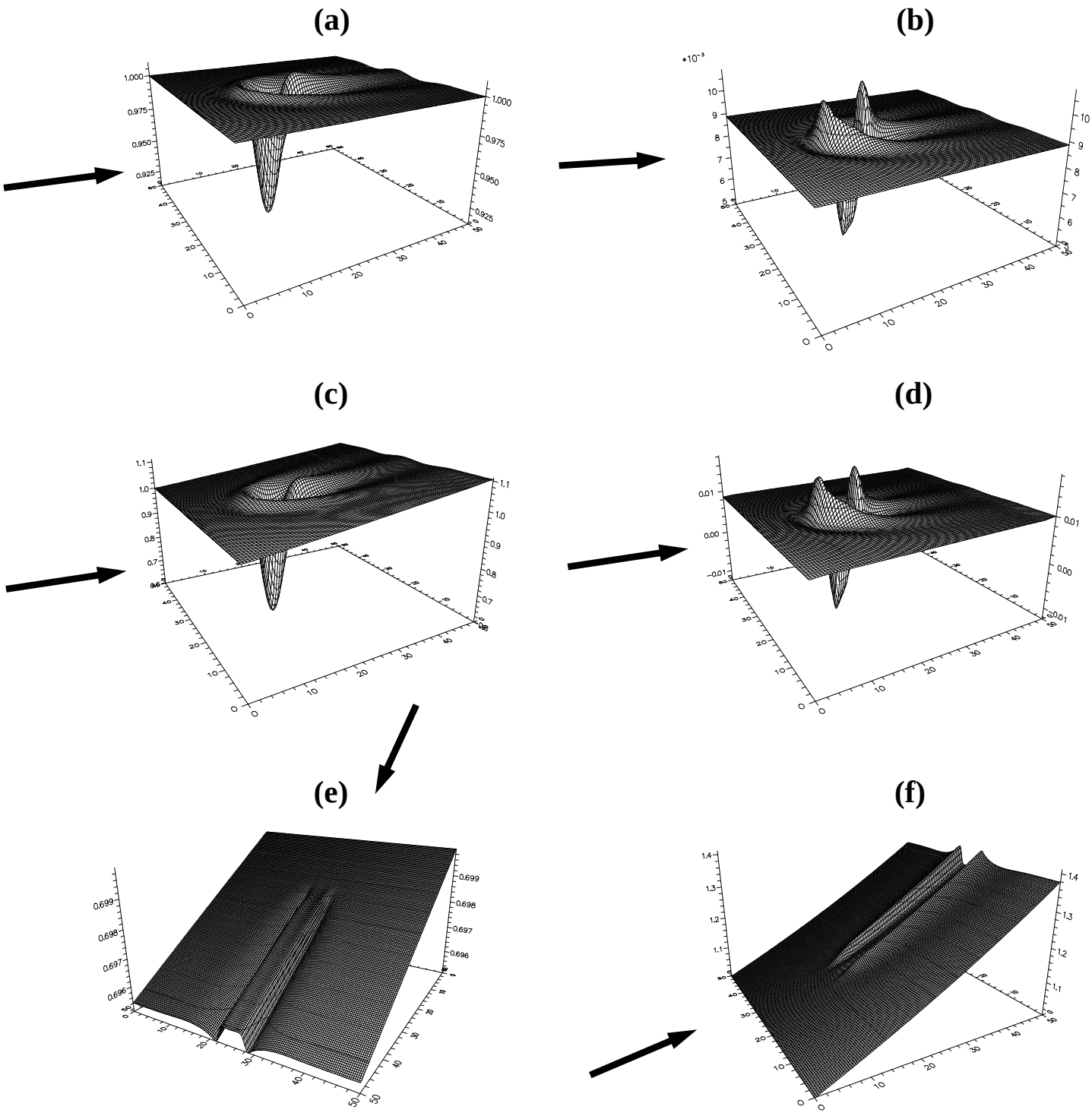
(a)
(b)
(c)
(d)
(e)
(f)

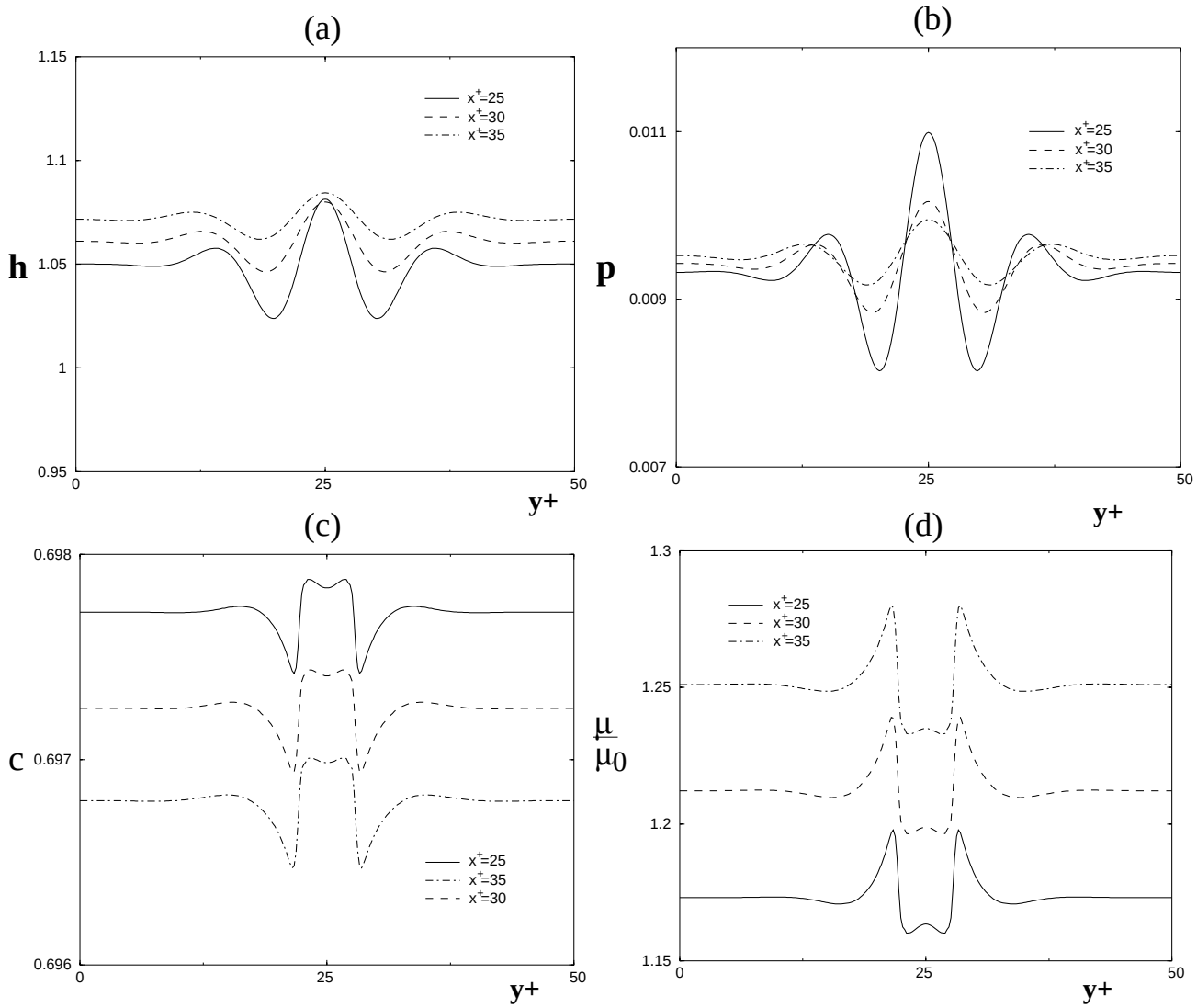
(a)
h
y+
x+=25
x+=30
x+=35
(b)
p
y+
x+=25
x+=30
x+=35
(c)
c
y+
x+=25
x+=35
x+=30
(d)
μ/μ0
y+
x+=25
x+=30
x+=35

(a)

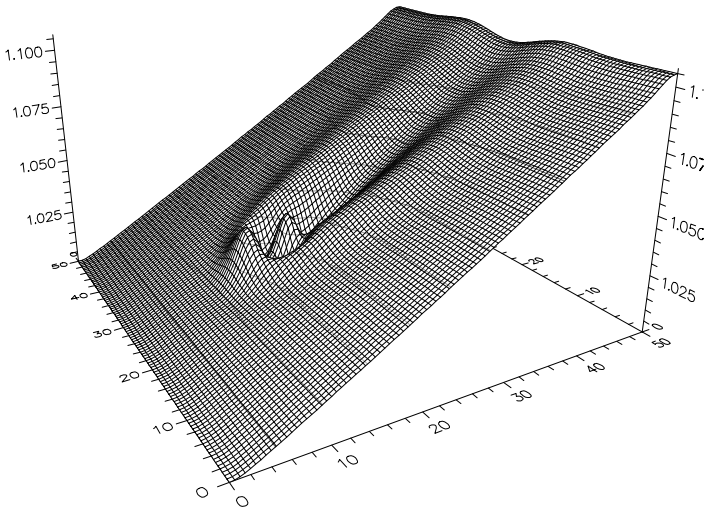
1.100
1.075
1.050
1.025
0
10
20
30
40
50

(b)

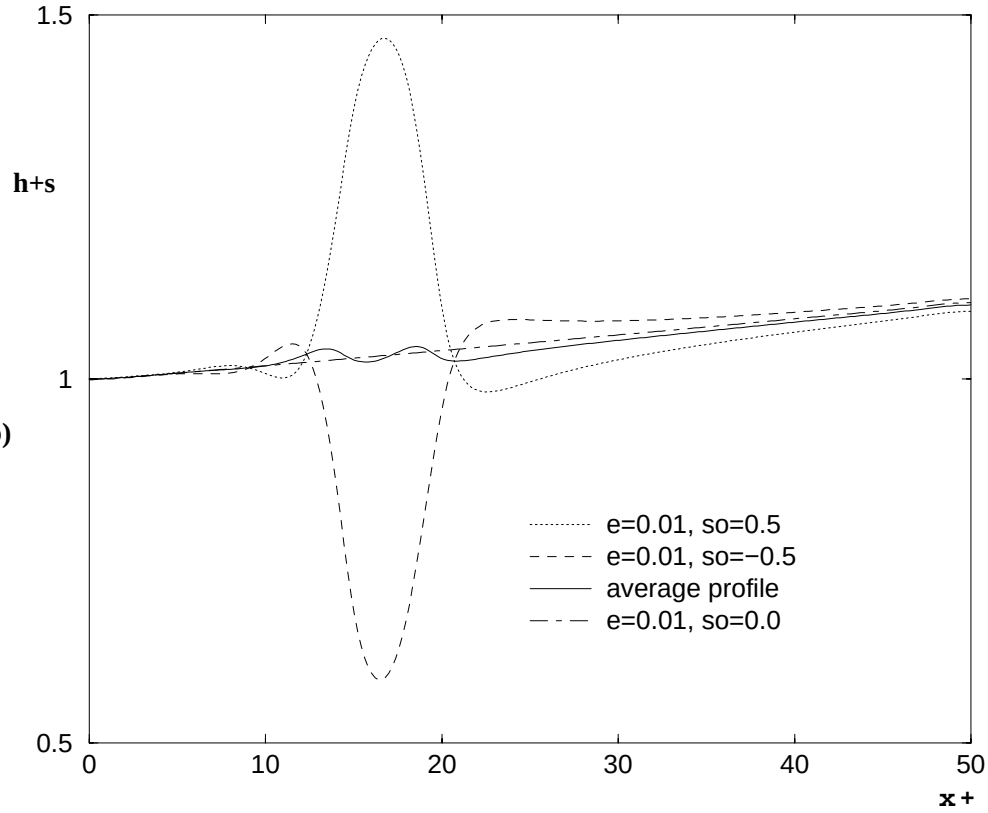
1.5
h+s
1
0.5
0
10
20
30
40
50
x+
e=0.01, so=0.5
e=0.01, so=−0.5
average profile
e=0.01, so=0.0